PROCEEDINGS A

royalsocietypublishing.org/journal/rspa

Research

Cite this article: Yenen TB *et al*. 2025 Mineral phase changes during intervertebral disc degeneration. *Proc. R. Soc. A* **481**: 20240488.
https://doi.org/10.1098/rspa.2024.0488

Received: 11 July 2024
Accepted: 2 April 2025

Subject Areas:
chemical biology

Keywords:
minerals, phase, intervertebral disc, degeneration

Authors for correspondence:
Andy Brown
e-mail: a.p.brown@leeds.ac.uk
Paul Freeman
e-mail: pf266@cam.ac.uk

Mineral phase changes during intervertebral disc degeneration

Theresa Banu Yenen[1,†], William D. Thom[2,†], Ravin Jugdaohsingh[2], Sam Khan[1], Viviana Rojas Solano[1], Giulio Lampronti[3], Kate Hughes[1], Janire Saez[7,8,9], Davide Corbetta[1], Salih Eminağa[5], Giunio Bruto Cherubini[6], Jonathan J. Powell[2], Andy Brown[4] and Paul Freeman[1]

[1]Queen's Veterinary School Hospital, [2]Biomineral Research Group, Department of Veterinary Medicine, and [3]Department of Materials Science and Metallurgy, University of Cambridge, Cambridge, UK
[4]School of Chemical and Process Engineering, University of Leeds, Leeds, UK
[5]Dick White Referrals, Cambridgeshire, UK
[6]Department of Veterinary Sciences, University of Pisa, Pisa, Italy
[7]Microfluidics Cluster UPV/EHU, BIOMICs Microfluidics Group, Lascaray Research Center, University of the Basque Country UPV/EHU, Vitoria-Gasteiz, Spain
[8]Basque Foundation for Science, IKERBASQUE, Bilbao, Spain
[9]Bioaraba Health Research Institute, Microfluidics Cluster UPV/EHU, Vitoria-Gasteiz, Spain

GBC, 0000-0002-0189-382X; PF, 0000-0001-6326-5573

Intervertebral disc disease is a common cause of pain and neurological deficits known to be associated with degeneration and calcification of discs in humans and animals. Here, we analysed samples of herniated disc material and compared it to material taken from non-herniated discs following surgical treatment in dogs. Our clinical approach to these cases allowed collection of approximately 100 samples providing a unique opportunity for a substantial case-controlled

---

[†] Joint first authors.

Electronic supplementary material is available online at https://doi.org/10.6084/m9.figshare.c.7765060.

© 2025 The Authors. Published by the Royal Society under the terms of the Creative Commons Attribution License http://creativecommons.org/licenses/by/4.0/, which permits unrestricted use, provided the original author and source are credited.

THE ROYAL SOCIETY
PUBLISHING

Downloaded from https://royalsocietypublishing.org/ on 24 June 2025

Downloaded from https://royalsocietypublishing.org/ on 24 June 2025

study, an opportunity not available to the human neurosurgeon. We analysed all samples using Fourier transform infrared (FTIR) spectroscopy, as well as subsets of 10 samples by X-ray diffraction (XRD) and two samples by transmission electron microscopy (TEM). We show the majority of herniated samples have FTIR spectra consistent with the presence of crystalline hydroxyapatite (HAp), whereas most non-herniated discs showed spectra consistent with amorphous phosphate. XRD and TEM confirmed these findings and the two samples examined with TEM identified the amorphous material as amorphous calcium phosphate (ACP) nanoparticle clusters of approximately 20 nm diameter and the crystalline HAp as polycrystalline needles up to 100 nm in length. Our data suggest that the intervertebral disc degenerative process involves conversion of ACP into crystalline HAp, which might predispose a disc to herniate.

1. Introduction

Intervertebral disc disease is characterized by the degeneration of disc(s) that separate the bones of the spine leading to localized pain that frequently extends to the legs and arms. It affects approximately 5% of the population in high-income countries and costs the UK National Health Service an estimated £5 billion p.a. (source Manchester Metropolitan University). Moreover, the disease is not restricted to humans. Chondrodystrophic dogs, characterized by a short-legged conformation, such as the dachshund and French bulldog, are especially prone to frequent, severe disease.

The intervertebral disc of mammals consists of the inner gelatinous nucleus pulposus, the fibrous annulus fibrosus, which creates a border around the nucleus, and the cartilaginous endplates, which bind the disc to the adjacent vertebral bodies. The healthy nucleus pulposus contains mainly notochordal cells surrounded by a matrix rich in proteoglycan and collagen (type II) as well as hyaluronic acid, creating a high osmotic pressure leading to high water content [1–6]. Calcification of intervertebral discs, in both the annulus fibrosus and the nucleus pulposus, is seen in disc degeneration of dogs and humans [7–11]. In dogs, calcification is associated with disc extrusion [12,13], which can lead to paralysis and incontinence or even death, while in humans, it is associated with discogenic pain [14–16]. However, while calcification is well recognized in the pathogenesis of intervertebral disc disorders, the relationship of the mineral composition to clinical disease is not known.

At the cellular level, amorphous calcium phosphate (ACP) particles are benign but ectopic hydroxyapatite (HAp) crystals are pro-inflammatory so the mineral phase could well dictate outcomes in calcified discs [17]. Indeed, biological HAp has been found in both degenerated [18] human intervertebral discs and in joints of patients with osteoarthritis [19]. In addition, large crystal-sized HAp accumulations (80–130 nm) were found in ovine intervertebral discs and were considered to be related to ageing [20]. By contrast, little is known about the presence of ACP in intervertebral discs despite many studies supporting the possibility that ACP could be the precursor form of HAp in other biological situations such as bone formation [21–24].

During surgery for extruded intervertebral discs in dogs, in addition to removing herniated nucleus pulposus material from the vertebral canal, it is good practice to clear out non-extruded neighbouring discs, a process known as disc fenestration which has been shown to be prophylactic in preventing future extrusion [25,26]. This provides a unique opportunity to compare the mineral phase of the calcified deposits in a clinically degenerative situation with very closely matched non-extruded discs, in a way that is not ethically possible in humans.

Here, we found that the major mineral phase present in extruded canine discs is crystalline HAp, whereas a significant proportion of non-extruded discs in the same animals contain ACP, providing evidence that a switch from amorphous to crystalline calcification appears to precede and might possibly trigger disc extrusion.

Downloaded from https://royalsocietypublishing.org/ on 24 June 2025

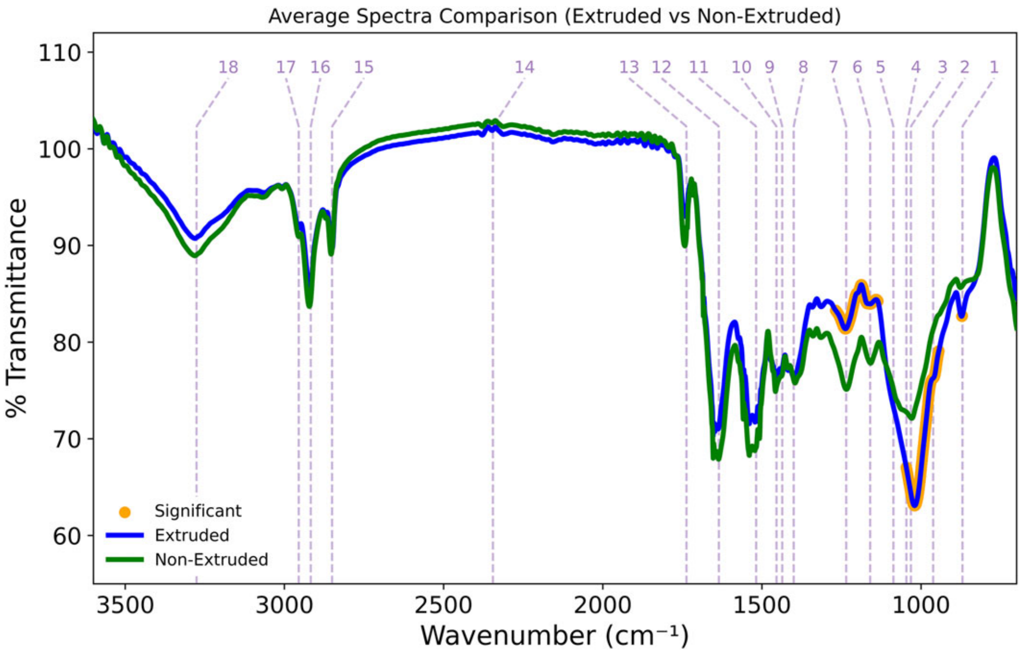

Figure 1. Group averaged FTIR spectra for extruded (blue, $n = 58$) and non-extruded (green, $n = 46$) intervertebral disc samples. Inter-group differences in transmittance were evaluated by two-sample t-tests; wavenumbers with Benjamini–Hochberg corrected (α 0.1%) p-values below 0.05 are highlighted (orange) and show consistent differences between extruded and non-extruded samples in (i) the carbonate v_2 peak (870 cm^{-1}), (ii) the phosphate peak region between 800 and 1100 cm^{-1} and (iii) the amide region between 1200 and 1300 cm^{-1}. Peak assignments are detailed in Table 1.

2. Results

In total, 57 clinical cases were included from 56 individual dogs (one dog suffered two separate episodes), all of which were chondrodystrophic or chondrodystrophic-mix dogs. Clinical details are contained in electronic supplementary material, table S1. The clinical cases generated 104 individual samples of intervertebral disc material, of which 58 were samples of extruded (herniated) material removed at surgical decompression, and 46 were non-extruded (control) samples of nucleus pulposus taken by fenestration of non-herniated discs.

(a) Fourier transform infrared analysis of intervertebral discs

Fourier transform infrared (FTIR) spectra of 104 disc samples, 58 extruded and 46 non-extruded, were produced. The raw data were afflicted with high-frequency noise and all spectra were pre-processed via wavelet denoising as described in the Materials and methods and as shown in electronic supplementary material, figures S2 and S3. No other pre-processing techniques, such as baseline normalization, were employed. Group average spectra were generated for the extruded and non-extruded sample groups (figure 1) and their transmittance profiles were found to overlay closely across much of the IR spectrum—aside from several key loci where pronounced inter-group differences were noted. Statistically significant inter-group spectral differences were found at (i) the carbonate (CO_3^{2-} ν_2) absorption band at 870 cm^{-1}, (ii) the phosphate absorption region between 950 and 1100 cm^{-1} (PO_4^{-3} ν_{3a-c} at 1030–1090 cm^{-1} and PO_4^{-3} ν_1 at 962 cm^{-1}), (iii) the glycosidic bond absorbance band at 1160 cm^{-1} and (iv) the amide absorption region between 1200 and 1300 cm^{-1}. Transmittance differences were also visible at the amide II (1518 cm^{-1}) and amide I (1635 cm^{-1}) regions, but these did not meet statistical significance after applying Benjamini–Hochberg correction.

Downloaded from https://royalsocietypublishing.org/ on 24 June 2025

Table 1. FTIR absorption peak assignments.

index	wavenumber (cm^{-1})	assignment	reference
1	870	carbonate, ν_2	[27,28]
2	962	phosphate, ν_1	[29]
3	1032	phosphate, ν_{3c}	[29]
4	1046	phosphate, ν_{3b}	[29]
5	1087	phosphate, ν_{3a}	[28,29]
6	1160	glycoside, C-O-C	[30]
7	1235	amide III	[30]
8	1400	carbonate, ν_3	[27,28]
9	1436	carbonate, ν_3/ν_4	[28]
10	1454	carbonate, ν_3/ν_4	[28]
11	1518	amide II	[31]
12	1635	amide I	[30]
13	1737	ester fatty acid, C=O	[30]
14	2345	carbon dioxide, ν_3	[32]
15	2850	aliphatic CH/CH2, ν_1	[30]
16	2917	aliphatic CH/CH2, ν_3	[30]
17	2955	aliphatic CH3, ν_3	[33]
18	3276	hydroxyl group, ν_3	[34]

Notably, the directionality of the inter-group absorption differences was not uniform. The extruded group average spectrum exhibited greater absorbance at the carbonate and phosphate loci and simultaneously reduced absorbance at the glycoside and amide loci. This finding was indicative of compositional sample differences between the groups and prompted close inspection of individual spectra at the significant wavenumber regions.

Case-by-case visual assessment revealed that while the vast majority of both extruded and non-extruded spectra contained a prominent PO_4^{-3} ν_3 peak suggesting the presence of calcium phosphate in both groups, the intensity and shape differed greatly between groups: 50 of 58 of the extruded spectra evinced a sharp PO_4^{-3} ν_3 peak, while only 10 of 46 non-extruded samples exhibited this peak shape. Furthermore, 47 of the 58 extruded spectra contained a distinct PO_4^{-3} ν_1 peak at approximately 960 cm^{-1}, while in the non-extruded group this vibration was only resolvable in seven of 46 samples. Since the PO_4^{-3} ν_1 peak at approximately 960 cm^{-1} is attributed specifically to phosphate vibrations in a crystalline (hydroxy)apatite environment [35], and PO_4^{-3} ν_3 signal was observable in the majority of samples, the disparity in PO_4^{-3} ν_1 intensity and resolvable features was suggestive of inter-group differences in mineral crystallinity.

To verify phosphate mineral spectral features, FTIR spectroscopy was conducted with reference calcium phosphate minerals, ACP and crystalline HAp. In accordance with Gadaleta *et al.* [35], this analysis revealed clear differences in the phosphate band signal structure (at 800–1100 cm^{-1})—the crystalline material evincing a sharper and more intense PO_4^{-3} ν_3 absorption peak (figure 2A) along with a distinct or well-resolved PO_4^{-3} ν_1 absorbance band and correspondingly pronounced maxima in the second derivative (figure 2B). Conversely, ACP exhibited a broad phosphate absorption band in the primary spectrum (figure 2A) and negligible second derivative signal at the expected PO_4^{-3} ν_3 and PO_4^{-3} ν_1 wavenumbers (figure 2B). Similar, albeit less extreme, differences in spectral profiles were also noted in the IR spectra of most extruded and non-extruded clinical samples, suggesting that extruded samples are more likely

Downloaded from https://royalsocietypublishing.org/ on 24 June 2025

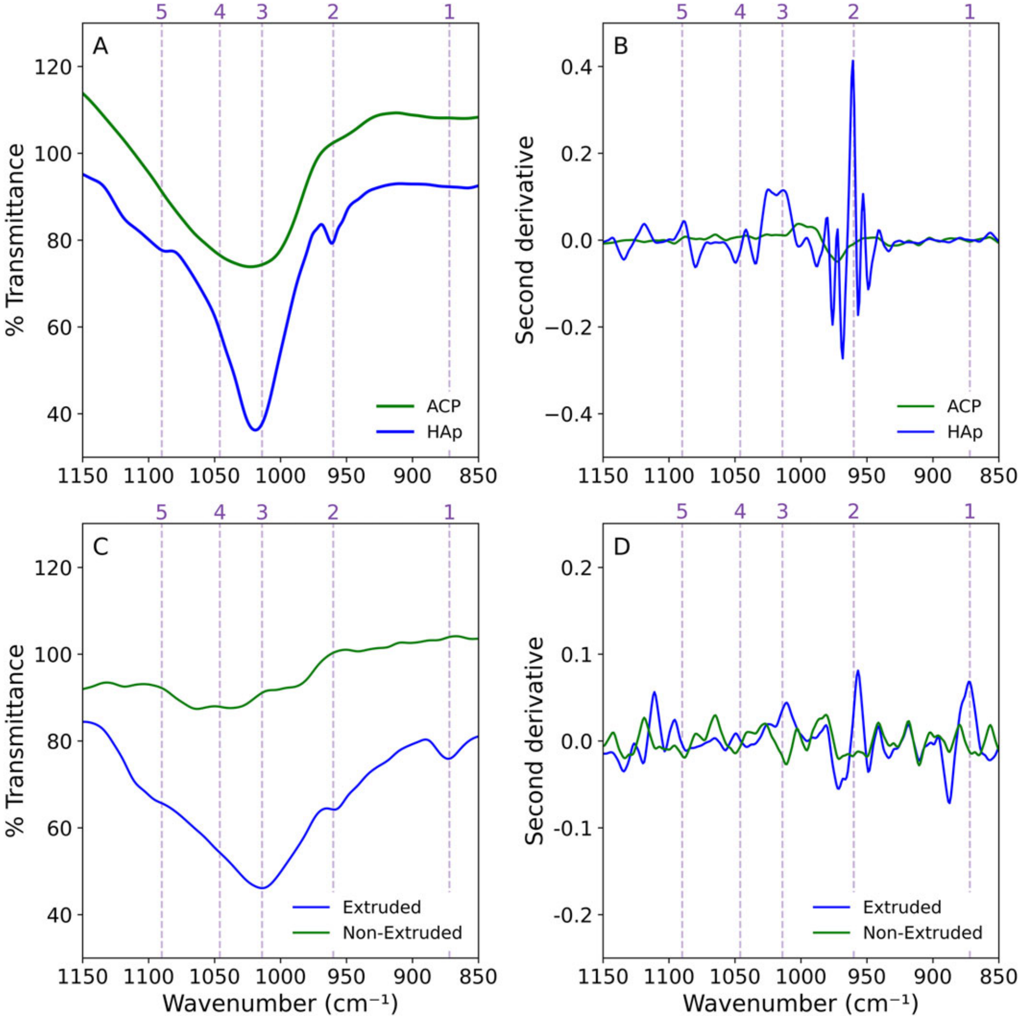

Figure 2. FTIR denoised spectral (A) and second derivative signal (B) comparison of the phosphate absorption region for non-crystalline and crystalline calcium phosphate mineral reference compounds, and for exemplar extruded and non-extruded clinical samples (C,D). The sharp PO_4 ν_1 signal (label 2; approx. 960 cm^1) in spectrum (A) and in the second derivative signal (B) is diagnostic for crystalline HAp and absent for ACP. This crystallinity marker is present in the extruded sample and not evident in the non-extruded sample (C,D). Peak labels are: (1) CO_3 ν_2, (2) PO_4 ν_1, (3) PO_4 ν_{3c}, (4) PO_4 ν_{3b} and (5) PO_4 ν_{3a}.

than their non-extruded counterparts to be abundant in the crystalline calcium phosphate mineral HAp (figure 2C,D at vertical line traces 2 and 3; electronic supplementary material, figure S4). Extruded samples also exhibited a distinct CO_3^{2-} ν_2 signal at 870 cm^{-1}, consistent with the presence of carbonated, biological HAp [36]. This feature was expectedly absent from the synthetic reference material.

To assess the second derivative signal at group level, peak amplitudes (in the second derivative spectra) were quantified at key wavenumbers for the CO_3^{2-} v_2, PO_4^{-3} v_1, PO_4^{-3} v_3, and amide peaks, and group probability density functions estimated via kernel density estimation (KDE) (figure 3). Consistent with the denoised spectral analysis reported above (figures 1 and 2), the second derivative spectra of extruded samples (blue) exhibited greater peak amplitudes at the CO_3^{2-} ν_2 (figure 3A) and PO_4^{-3} ν_1 (figure 2B) absorption bands than their non-extruded (orange) counterparts. This difference was particularly striking at the PO_4^{-3} ν_1 band (Welch's *t*-test *p*-value

Downloaded from https://royalsocietypublishing.org/ on 24 June 2025

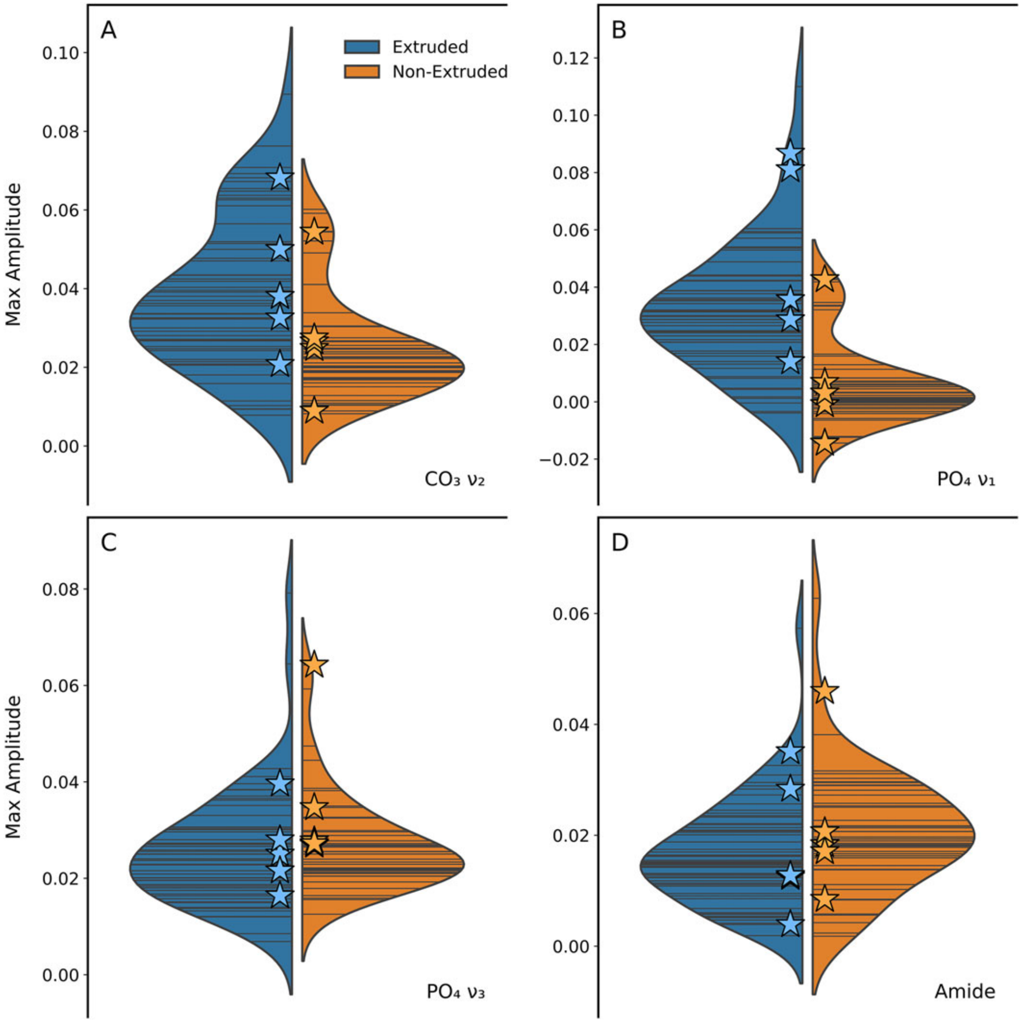

Figure 3. Violin plots displaying the distribution of FTIR spectra second derivative maximum amplitude values for extruded (blue) and non-extruded (orange) samples across four vibrational regions (A) CO_3^{2-} ν_2, (B) PO_4^{-3} ν_1, (C) PO_4^{-3} ν_3 and (D) amide. The width of each violin indicates the KDE, representing the probability density of the data at different amplitude values. Internal stick lines represent the individual observations within each category, while the overlaid star markers highlight the specific samples down-selected for XRD analysis. The density is normalized by count to reflect the number of observations in each region. A statistically significant difference between extruded and non-extruded samples was found in the PO_4^{3-} ν_1 region (subplot b; $p = 0.0483$, Welch's t-test).

0.048), where 50 of 58 extruded samples had a second derivative peak amplitude (median 0.033 units) greater than the upper quartile value (0.018 units) of the non-extruded samples (median 0.007 units). The PO_4^{-3} ν_1 second derivative peak amplitudes of the non-extruded samples appeared to exhibit a bimodal distribution, with greatest density at ca. zero units and a smaller subsidiary probability peak at 0.04 units. In contrast to the CO_3^{2-} ν_2 and PO_4^{-3} ν_1 derivative data, and despite large differences in group average spectra absolute signal intensity (figure 1), second derivative peak amplitudes at the ν_3 PO_4^{-3} (figure 3C) and amide (figure 3D) absorbance regions were similar for both groups—indicating the presence of similar compositional components in both groups.

The second derivative analyses accorded with findings from visual spectral classification, indicating a substantial inter-group difference in the frequency of samples containing detectable

Downloaded from https://royalsocietypublishing.org/ on 24 June 2025

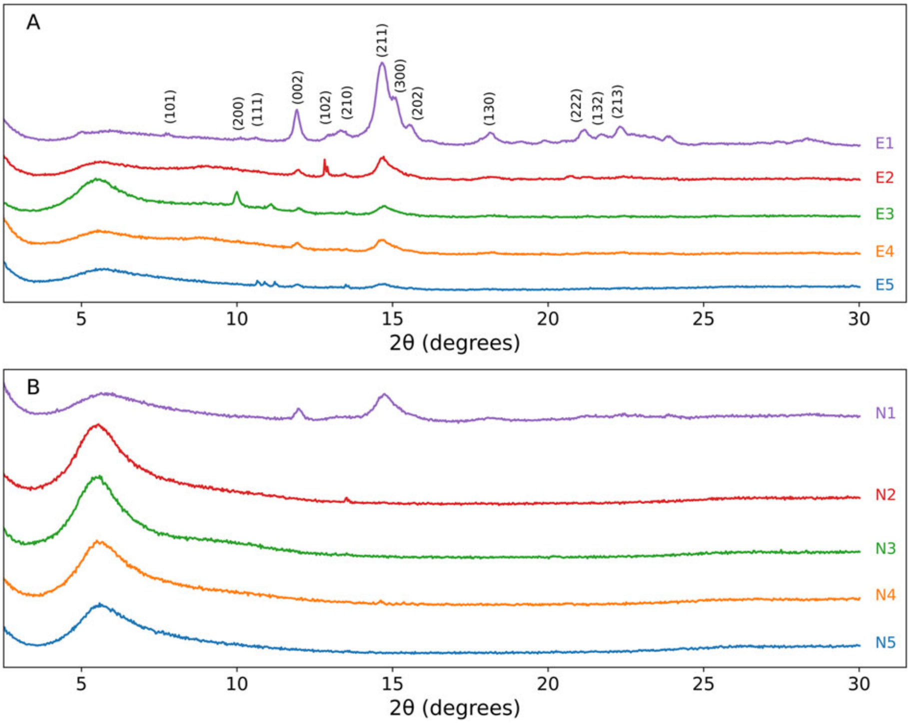

Figure 4. Powder X-ray diffraction patterns of representative extruded (A) and non-extruded (B) samples, indexed against hydroxyapatite reference structure ICDD 74-0565. All extruded samples E1–E5 and one non-extruded sample (N1) have crystalline hydroxyapatite peaks, while the remaining non-extruded samples (N2–N5) are all X-ray amorphous.

crystalline HAp. Notably, intra-group spectral differences were also sustained, with a sub-population of non-extruded controls appearing to exhibit crystalline spectral features too.

To corroborate the spectroscopic analyses and confirm the presence/absence of crystalline material, a series of samples from both groups (extruded and non-extruded) were selected for X-ray diffraction (XRD). These samples (figure 3, star markers) were selected based on the second derivative distributions of both groups, in order to represent the range of spectral profiles displayed and especially to ensure that distinct sample sub-populations (e.g. non-extruded PO$_4^{-3}$ v_1 low-signal versus high-signal within each group) were represented.

(b) Powder X-ray diffraction results

Five extruded and five non-extruded discs were selected for XRD analysis because they were considered to be representative of the range of second derivative maxima signal at the PO$_4^{-3}$ v_3, PO$_4^{-3}$ v_1 and CO$_3^{2-}$ v_2 functional group regions of the FTIR spectra of the 58 extruded and 46 non-extruded tested above (figure 3). The XRD profiles of all five of the extruded (figure 4A, traces E1–E5) and one of the five non-extruded disc materials (figure 4B, trace N1) were indicative of crystalline HAp by the presence of significant 2θ peaks at around 15°, indexed according to the Inorganic Crystal Structure Database file 74-0565 [37]. Phase identification was confirmed via structural Rietveld refinements. The details of the powder X-ray diffraction (PXRD) data fitting strategy are reported in the electronic supplementary material together with the Rietveld plots for all the samples containing a crystalline fraction (electronic supplementary material, figures S5–S10). The other four non-extruded samples showed profiles without any significant Bragg peaks indicating that these contained amorphous material only (figure 4B, traces N2–N5; electronic supplementary material, figure S11). Structural and microstructural parameters as obtained from

Downloaded from https://royalsocietypublishing.org/ on 24 June 2025

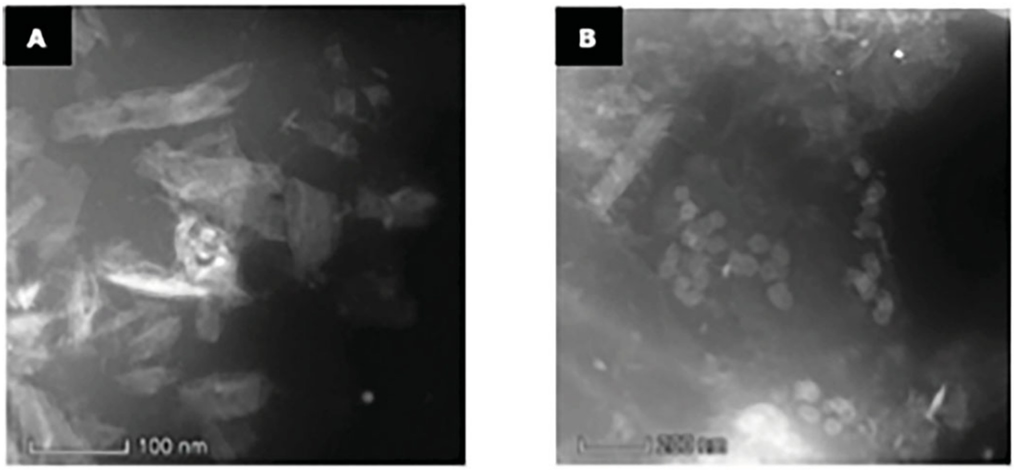

Figure 5. HAADF-STEM images of the extruded disc (A) material showing agglomerate of needles indicative of hydroxyapatite nanocrystals (A) and non-extruded (B) disc material showing small amorphous spheres and only some needle-like particles. Scale marker bars are 100 nm and 200 nm in A and B, respectively.

the refinements are reported in electronic supplementary material, table S2. Crystal sizes of the crystalline HAp mineral fraction in the extruded specimens ranged from 10 to 15 nm, as estimated by sample contribution to diffraction peak broadening by implementing the Scherrer equation in the whole-pattern analysis (electronic supplementary material, table S2 and figures S5–S10).

Importantly, the non-extruded sample that contains crystalline HAp (figure 4B, trace N1; electronic supplementary material, figure S10) was the sample selected to represent the non-extruded PO_4^{-3} v_1 positive sub-population (figure 3B, highest orange star), supporting the sensitivity of that spectral feature for HAp detection across clinical groups. The crystallite size for this sample is estimated to be less than 8 nm (electronic supplementary material, table S2), slightly smaller than the crystallite size range of the extruded samples.

(c) Electron microscopy analysis of two representative samples

TEM analysis of one extruded (E2) and one non-extruded (N3) intervertebral disc sample was supportive of both the FTIR and XRD findings. STEM images of the extruded disc material revealed a continuous, gel-like or amorphous phase containing many nanoscale, needle-like agglomerates or deposits within the matrix (figure 5A; the crystalline needles scatter more strongly than the amorphous matrix and so have a white contrast in the HAADF images (see also electronic supplementary material, figure S12a,b). STEM-EDX elemental analysis indicated that the needle-like agglomerates were Ca, P and O rich (electronic supplementary material, figure S13). Furthermore, electron diffraction of the extruded sample showed four polycrystalline rings of spacing 2.82 (strong ring), 3.2, 3.5 and approximately 4.4 Å consistent with those expected for HAp [36] (figure 6A).

STEM images of the non-extruded disc material revealed gel-like deposits similar to the extruded sample. The deposits within the matrix consisted of nanoscale, spherical agglomerates identified as amorphous material by (i) the weaker scattering in the image (figure 5B; the deposits are smaller, rounder and less white than the needles in the extruded material in figure 5A) and (ii) no visible atomic lattice in high-resolution imaging (electronic supplementary material, figure S12c,d). In addition, electron diffraction analysis confirmed that the deposits in the gel are predominately amorphous by a lack of sharp rings and spots (figure 6B). The spherical agglomerates in the non-extruded sample that were amorphous by electron diffraction were found to be Ca, P and O rich by energy dispersive X-ray spectroscopy (EDX), consistent with an ACP phase (electronic supplementary material, figure S14).

Downloaded from https://royalsocietypublishing.org/ on 24 June 2025

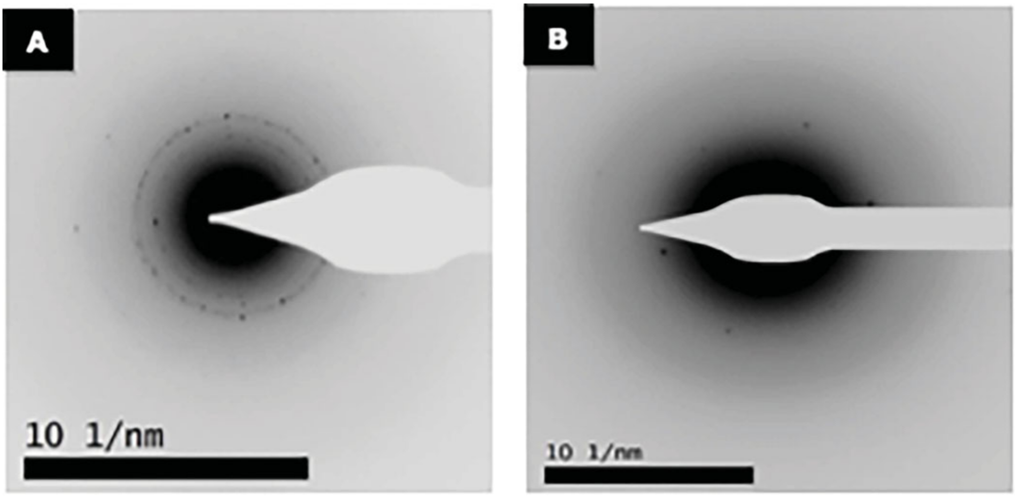

Figure 6. Electron diffraction pattern of extruded (A) and non-extruded (B) intervertebral disc material note. (A) Electron diffraction pattern of extruded IVD material shows four rings at 2.82 (strong ring), 3.2, 3.5 and approximately 4.4 Å for which the ring spacings are indicative of hydroxyapatite (see text). (B) Electron diffraction pattern of non-extruded IVD material showing diffuse rings with very few diffraction spots that indicate the tested material is predominately amorphous. The scale marker bars are 10 nm^{-1} in both patterns shown.

3. Discussion

This study produces new information regarding the mineral form of calcified degenerate intervertebral discs in 56 chondrodystrophic dogs, revealing that the discs contain either crystalline HAp or ACP nanoparticles. ACP nanoparticles were found only in discs that had not undergone extrusion (or herniation), whereas crystalline HAp was found in both herniated and non-herniated discs. These findings suggest that canine intervertebral disc degeneration, at least in this group of chondrodystrophic dogs, involves a transformation (change of phase) from an initially ACP phase into crystalline HAp nanoparticles. It is possible that this phase change may then predispose the discs to extrusion.

To minimize the possibility of mineral phase changes post-sample collection, freeze-drying was used for sample preparation prior to analysis. Freeze-drying has been shown to conserve the phase and morphology of minerals, although it can cause particle size reduction [27]. It is also possible that the mineral phase of samples of nucleus pulposus changed following extrusion, i.e. once inside the vertebral canal and outside the disc, a possibility that could be tested in the future by comparing nuclear material remaining within an extruded disc with the herniated, extruded material. This, however, seems unlikely given that some non-extruded samples also contained crystalline material.

In this study, all 102 samples were analysed by FTIR spectroscopy to demonstrate statistical differences in the second derivative maxima signals of the phosphate band at 800–1100 cm^{-1} that suggest the extruded disc material contained crystalline HAp (figures 2 and 3). A sample set of five extruded and five non-extruded discs shown to be representative of this FTIR spectroscopy analysis was taken forward for XRD measurement (figure 4). Results confirmed the findings that ACP nanoparticles were found only in discs which had not undergone extrusion, whereas crystalline HAp was found in all five extruded discs and one non-extruded disc. A single sample from each XRD group, which from visual evaluation of FTIR spectra appeared representative of the bulk of samples from each group (figure 3), were further submitted for transmission electron microscope analysis to reveal the nanoscale phase and internal structure of the investigated materials (figure 5) and to confirm that when crystalline the HAp phase forms needles (figures 5 and 6).

Downloaded from https://royalsocietypublishing.org/ on 24 June 2025

A small number of FTIR spectra from the extruded samples did not reveal any of the prominent phosphate or carbonate peaks consistent with the presence of biological HAp [28–31]. Although it is possible that these extruded samples were not calcified or did not include crystalline HAp, it is more likely that a sampling error in surgery might be the reason for these findings, given the clinical nature of this study.

Crystal sizes in the samples analysed by XRD were in the range of 5–15 nm in the five extruded and the single non-extruded sample, in line with previously reported crystal sizes for biological HAp [32]. The size of the crystalline needles observed by TEM was bigger (50–100 nm) suggesting these are polycrystalline agglomerates (that could have grown from the smaller ACP particles seen in the non-herniated disc material). Previous literature suggests that the size of the crystalline particles of HAp in bone increases with maturity [31,33,34]. It is possible that crystal, and agglomerate sizes of the HAp within the intervertebral discs increases with the stage of degeneration, and may also be associated with extrusion, but larger sample size analysis is required to make a more definitive statement regarding this.

A few of the non-extruded samples showed FTIR spectra consistent with crystalline HAp (and one had an XRD pattern confirming this; N1 in figure 4). This is not unexpected if the degenerative process involves a transformation of ACP to crystalline HAp prior to extrusion, since it may be that a critical mass and/or size of HAp is needed before herniation/extrusion occurs. Clearly, it is likely that multiple other factors such as mechanical stress, dehydration and loss of proteoglycans and genetic predisposition are also involved in intervertebral disc disease and herniation [38]. However, if discs containing crystalline HAp could be identified before they have herniated, e.g. by calibration to MRI, it may be possible to target them with a prophylactic therapy such as surgical fenestration, chemonucleolysis or laser ablation [25,26,38,39].

This study sheds some light on the process of calcification that is an important part of intervertebral disc degeneration in dogs and people and has been associated with disease in both species. Our findings lead us to speculate that calcification is a process in which initially an ACP phase is formed within the nucleus pulposus, and that this then transforms into a crystalline HAp. This is not unexpected given what is known about the maturation of bone and teeth and the role of HAp in these biological materials. We can only speculate, at this stage, on why the calcium phosphate undergoes such a phase change; possibly, it is associated with the loss of a stabilizing substance that maintains the amorphous phase only until a certain level of degeneration of the disc.

A recent review of the role of calcification in human intervertebral disc disease also points to the role of calcium pyrophosphate [11], but we did not identify this specific material in our samples. There may indeed be some differences in the pathological process between dogs and humans, although it is clear that calcium has a significant role in intervertebral disc disease in both species, with canine intervertebral disc disease having been suggested to be a good natural model of the disease in humans [40]. If our hypothesis regarding the maturation of the calcification in intervertebral discs is correct, it may further be possible to intervene in this process to slow down or even prevent or reverse the process and perhaps reduce the rate of intervertebral disc herniation as a result.

Further investigation into the topographical and mechanical properties of intervertebral disc samples is needed to better describe and verify these findings, as well as attempt to define the biomechanical features of intervertebral disc material.

4. Conclusion

Our results shed new light on the process of calcification in intervertebral disc degeneration and disease. It appears that an ACP phase within discs is transformed into crystalline HAp, and this might either be due to an unidentified trigger or to the loss of a stabilizing agent. This change in the mineral phase within the intervertebral disc appears to be associated with herniation of the disc, perhaps due to alterations in biomechanical properties. The identification of this transformation as an integral part of the degenerative process requires further verification

Downloaded from https://royalsocietypublishing.org/ on 24 June 2025

potentially by analysis of a larger number of samples with techniques such as XRD and TEM (as illustrated here), but if confirmed opens up the possibility for further work, which might lead to new therapies and/or prophylactic measures to treat and/or reduce the incidence of this frequently disabling disease in both humans and dogs.

5. Material and methods

(a) Inclusion criteria

The study population consisted of chondrodystrophic dogs with intervertebral disc extrusion that underwent surgical treatment at two different institutions, the Queen's Veterinary School Hospital, University of Cambridge and Dick White Referrals, Newmarket, between October 2020 and June 2021. Dogs were included if they had a diagnosis of intervertebral disc extrusion made by either magnetic resonance imaging (MRI) or computed tomography (CT) and confirmed surgically. Details recorded for each case included breed, age, sex and location of extrusion. The study was approved by the Ethics and Welfare Committee of the Department of Veterinary Medicine, University of Cambridge, and all methods were performed in accordance with the relevant guidelines and regulations. The study is reported in accordance with relevant ARRIVE guidelines. All data associated with this paper are openly available from the University of Cambridge Data Repository.

(b) Study and control samples

Study samples consisted of extruded disc material collected during decompressive surgery. Material was collected directly from the surgically exposed vertebral canal by physical extraction with a variety of instruments following laminectomy performed with a high-speed burr [41].

Control samples consisted of material collected during prophylactic fenestration of adjacent non-extruded discs [42,43]. These discs were confirmed to be non-extruded following examination of their imaging (MRI or CT). Both extruded and non-extruded disc materials were placed into sterile plain plastic sample pots and held at +4°C for a maximum of 48 h. They were then transferred and stored in a –20°C freezer until the freeze-drying process.

If the sample was large enough, half of the collected material was separated for histopathology. These samples were fixed in 10% formalin for 24–48 h and then transferred into pots with 70% ethanol until histopathologic investigation. For slide preparation, samples were embedded in paraffin wax, cut to thicknesses of 4–5 µm, and stained with haematoxylin and eosin. None of the samples were decalcified during preparation. Slides were then observed with an optical microscope at a magnification of 40× and were evaluated by a European Boarded Anatomic Pathologist. Twenty-seven samples, of which 21 were extruded and six were non-extruded, were evaluated in this way, and all were identified as nucleus pulposus because they contained notochordal cells and/or chondrocyte-like cells.

(c) Sample preparation

All samples were freeze-dried prior to mineral analysis for a total of 17 h. After placing into the freeze-dryer (VirTis Advantage Plus), they were cooled from +5°C to −35°C at a rate of $-0.19^{\circ}\mathrm{C\,min^{-1}}$ and at a pressure of 400 mTorr. This was followed by the drying phase, where the temperature was gradually increased to +20°C while the pressure was held at 80 mTorr. Samples were then brought to room temperature and stored until mineral analysis.

(d) Fourier transform infrared analysis

FTIR analysis was performed with a Shimadzu IRPrestige21 Fourier Transform Infrared Spectrophotometer equipped with a Golden Gate ATR accessory (Specac Ltd.). FTIR scans of

Downloaded from https://royalsocietypublishing.org/ on 24 June 2025

samples covered wavenumbers 400–4000 cm^{-1}. The spectrometer was set to a scan speed of 2.8 $\mathrm{mm\,s}^{-1}$ and had a resolution of 2 cm^{-1}. The ATR sample holder was cleaned twice with 100% ethanol between each sample analysis. Samples were analysed in the form they left the freeze-drying process, with no grinding or further handling/sample prep. Due to the small size of the ATR sample holder and the lack of sample homogeneity, most samples (i.e. where possible) were subsampled up to three times and each scan recorded. For samples with multiple scans, when the three spectra differed (21 of 104 samples), the best-conditioned spectrum was included in the data analysis, with selection considering the following factors: baseline stability, degree of high-frequency noise and resolution of the phosphate absorbance region (900–1200 cm^{-1}).

(e) Interpretation of Fourier transform infrared spectra of intervertebral discs

All FTIR spectra were treated via wavelet denoising using the PyWavelets library in Python, employing the coif5 wavelet, with level 3 decomposition, and hard thresholding at threefold of the Universal Threshold (see electronic supplementary material, figure S3 and figure S15 for Python code). Group average spectra were calculated for extruded and non-extruded samples by averaging the denoised spectra across all samples within each group. Two-sample *t*-tests were performed at each wavenumber to identify statistically significant differences between the groups. The assumption of unequal variances was applied. To account for multiple comparisons, the *p*-values were corrected using the Benjamini–Hochberg false-discovery rate method with an α threshold of 0.0001.

Thereafter, second derivative analysis was performed at absorbance regions which had been identified as significantly differing between the average spectra of the two clinical groups, namely: CO_3^{-2} ν_3 (865–890 cm^{-1}), PO_4^{-3} ν_1 (955–965 cm^{-1}), PO_4^{-3} ν_3 (1015–1095 cm^{-1}) and amide (cm^{-1}) absorbance bands. KDE was applied to visualize the distribution of maximum amplitude values across sample groups using a Gaussian kernel for smoothing. The bandwidth for the KDE was automatically selected using Scott's rule, adjusting the level of smoothing based on the data distribution. Violin plots were generated using seaborn, with width scaled according to the number of observations. Welch's *t*-test was used to test the statistical significance of inter-group differences in second derivative peak amplitude at critical loci. Before each statistical test/analysis, a Shapiro–Wilk test was performed to confirm that the data were normally distributed.

(f) Calcium phosphate mineral reference compounds

Hydroxyapatite reference material, calcium chloride, magnesium chloride, disodium phosphate and tris buffer were all obtained from Sigma-Aldrich. Hydroxyapatite reference material was used as received without modification, while ACP was synthesized. Since ACP is metastable to HAp and undergoes mineral transformation rapidly at room temperature the following procedure was employed to prepare it: to 45 ml of tris (300 $\mathrm{mMol\,l}^{-1}$) buffered (pH 9.09) disodium phosphate solution (110 $\mathrm{mMol\,l}^{-1}$), 5 ml of tris (300 $\mathrm{mMol\,l}^{-1}$) buffered (pH 8.09) calcium solution, containing calcium chloride (800 $\mathrm{mMol\,l}^{-1}$) and magnesium chloride (200 $\mathrm{mMol\,l}^{-1}$) was added under vigorous stirring. The resulting precipitates were immediately collected by centrifugation, washed three times in ice-cold pH 9 water, three times in ice-cold acetone, dried under vacuum and then stored at −80°C. Both the reference materials were analysed with XRD to verify that they were comprised from the appropriate mineral phase.

(g) X-ray diffraction

PXRD analysis was performed on five extruded (study) and five non-extruded (control) samples that were previously analysed by FTIR spectroscopy. Samples were selected to represent the group ranges of FTIR spectral profile, comprising datum at the modes, upper and lower ends of the second derivative distributions. In particular, since the non-extruded samples exhibited a

Downloaded from https://royalsocietypublishing.org/ on 24 June 2025

bimodal distribution in second derivative amplitude at the critical PO_4^{-3} ν_1 absorbance band, we ensured that both sub-populations were represented in the XRD analyses—one sample (N1) was taken from the high-signal non-extruded subgroup and the other four from across the low-signal subgroup. The freeze-dried disc materials were gently crushed with an agate pestle & mortar and placed on a low background sample holder made of silicone. PXRD data were collected in Bragg–Brentano geometry with a Bruker D8 Advance diffractometer equipped with a Mo Kα radiation source, and a Lynxeye XE-T linear position sensitive detector with the following parameters: 2θ range: 5–40°; step size 0.015°; time per step 1 s; 50 kV × 40 mA.

(h) Transmission electron microscopy analysis

Transmission electron microscopy (TEM) was performed on two representative samples (one extruded and one non-extruded), after they had been freeze-dried and analysed with FTIR spectroscopy and XRD. A Thermo Fisher Scientific Helios G4 CX scanning electron microscope was used for scanning electron microscopy energy dispersive X-ray (SEM-EDX) analysis, and a Thermo Fisher Scientific Titan [3] Themis G2 SuperX 300 kV scanning TEM with a Gatan OneView camera was used for TEM, scanning transmission electron microscopy (STEM), energy dispersive X-ray spectroscopy (STEM-EDX) and electron diffraction analysis.

SEM-EDX was initially performed on the extruded sample to determine the elements present in the material before any further sample preparation. A small amount of each of the two freeze-dried disc materials was then suspended in methanol after grinding in a pestle and mortar before being directly drop-cast onto a holey carbon TEM support film (EM Resolutions Ltd.) and air-dried. TEM images of the disc materials were generated with high-angle annular dark-field imaging by scanning transmission electron microscopy (HAADF-STEM). In addition, electron diffraction patterns were obtained for both samples using a selected area aperture of approximately 200 nm diameter at the image plane. Furthermore, STEM-EDX analysis was performed for elemental mapping (data acquired and processed in the Thermo software Velox).

(i) Raw data

Raw data are available upon request.

Ethics. Ethical approval for this study was given by the Welfare and Ethics Committee of the Dept of Veterinary Medicine, University of Cambridge CR442. The study was approved by the Ethics and Welfare Committee of the Department of Veterinary Medicine, University of Cambridge, and all methods were performed in accordance with the relevant guidelines and regulations. The study is reported in accordance with relevant ARRIVE guidelines. All data associated with this paper are openly available from the University of Cambridge Data Repository.

Data accessibility. All raw data are available upon request and are deposited in full in data repository and as electronic supplementary material [44].

Declaration of AI use. We have not used AI-assisted technologies in creating this article.

Authors' contributions. T.B.Y.: writing—original draft; W.D.T.: data curation, formal analysis, writing—review and editing; R.J.: investigation, methodology, writing—review and editing; S.K.: data curation, formal analysis, writing—review and editing; V.R.S.: data curation, investigation; G.L.: formal analysis, methodology, writing—review and editing; K.H.: methodology; J.S.: methodology, writing—review and editing; D.C.: investigation, methodology, writing—review and editing; S.E.: investigation, writing—review and editing; G.B.C.: methodology, writing—review and editing; J.J.P.: conceptualization, methodology, writing—review and editing; A.B.: formal analysis, investigation, methodology, writing—review and editing; P.F.: conceptualization, funding acquisition, writing—review and editing.

All authors gave final approval for publication and agreed to be held accountable for the work performed therein.

Conflict of interest declaration. We declare we have no competing interests.

Funding. Work was part-funded by a grant from the Alice Noakes Trust, UK.

Downloaded from https://royalsocietypublishing.org/ on 24 June 2025

References

1. Bergknut N, Smolders LA, Grinwis GCM, Hagman R, Lagerstedt A-S, Hazewinkel HAW, Tryfonidou MA, Meij B. 2013 Intervertebral disc degeneration in the dog. Part 1: anatomy and physiology of the intervertebral disc and characteristics of intervertebral disc degeneration. *Vet. J.* **195**, 282–291. (doi:10.1016/j.tvjl.2012.10.024)
2. Cole TC, Burkhardt D, Frost L, Ghosh P. 1985 The proteoglycans of the canine intervertebral disc. *Biochim. Biophys. Acta* **839**, 127–138. (doi:10.1016/0304-4165(85)90029-7)
3. Cole TC, Ghosh P, Taylor TKF. 1986 Variations of the proteoglycans of the canine intervertebral disc with ageing. *Biochim. Biophys. Acta* **880**, 209–219. (doi:10.1016/0304-4165(86)90082-6)
4. Hansen HA. 1952 Pathologic-anatomical study on disc degeneration in dog, with special reference to the so-called enchondrosis intervertebralis. *Acta Orthop. Scand. Suppl.* **11**, 1–117. (doi:10.3109/ort.1952.23.suppl-11.01)
5. Hansen T, Smolders LA, Tryfonidou MA, Meij BP, Vernooij JCM, Bergknut N, Grinwis GCM. 2017 The myth of fibroid degeneration in the canine intervertebral disc: a histopathological comparison of intervertebral disc degeneration in chondrodystrophic and nonchondrodystrophic dogs. *Vet. Pathol.* **54**, 945–952. (doi:10.1177/0300985817726834)
6. Rosenblatt AJ, Bottema CDK, Hill PB. 2014 Radiographic scoring for intervertebral disc calcification in the dachshund. *Vet. J.* **200**, 355–361. (doi:10.1016/j.tvjl.2014.03.023)
7. Gruber H, Norton HJ, Sun Y, Hanley EN. 2007 Crystal deposits in the human intervertebral disc: implications for disc degeneration. *J. Spine* **7**, 444–450. (doi:10.1016/j.spinee.2006.08.015)
8. Karamouzian S, Eskandary H, Faramarzee M, Saba M, Safizade H, Ghadipasha M, Malekpoor AR, Ohadi A. 2010 Frequency of lumbar intervertebral disc calcification and angiogenesis, and their correlation with clinical, surgical, and magnetic resonance imaging findings. *J. Spine* **35**, 881–886. (doi:10.1097/BRS.0b013e3181b9c986)
9. Shao J, Yu M, Jiang L, Wei F, Wu F, Liu Z, Liu X. 2016 Differences in calcification and osteogenic potential of herniated discs according to the severity of degeneration based on Pfirrmann grade: a cross-sectional study. *BMC Musculoskelet. Disord.* **17**, 191. (doi:10.1186/s12891-016-1015-x)
10. Smolders LA, Bergknut N, Grinwis GCM, Hagman R, Lagerstedt A-S, Hazewinkel HAW, Tryfonidou MA, Meij BP. 2013 Intervertebral disc degeneration in the dog. Part 2: chondrodystrophic and non-chondrodystrophic breeds. *Vet. J.* **195**, 292–299. (doi:10.1016/j.tvjl.2012.10.011)
11. Zehra U, Tryfonidou M, Iatridis JC, Illien-Jünger S, Mwale F, Samartzis D. 2022 Mechanisms and clinical implications of intervertebral disc calcification. *Nat. Rev. Rheumatol.* **18**, 352–362. (doi:10.1038/s41584-022-00783-7)
12. Rohdin C, Jeserevic J, Viitmaa R, Cizinauskas S. 2010 Prevalence of radiographic detectable intervertebral disc calcifications in Dachshunds surgically treated for disc extrusion. *Acta Vet. Scand.* **52**, 1–7. (doi:10.1186/1751-0147-52-24)
13. Stigen Ø, Ciasca T, Kolbjørnsen Ø. 2019 Calcification of extruded intervertebral discs in dachshunds: a radiographic, computed tomographic and histopathological study of 25 cases. *Acta Vet. Scand.* **61**, 1–9. (doi:10.1186/s13028-019-0448-2)
14. Azizaddini S, Arefanian S, Redjal N, Walcott BP, Mollahoseini R. 2013 Adult acute calcific discitis confined to the nucleus pulposus in the cervical spine: case report. *J. Neurosurg. Spine* **19**, 170–173. (doi:10.3171/2013.4.SPINE12906)
15. Nogueira-Barbosa MH, Da Silva Herrero CF, Pasqualini W, Defino HL. 2013 Calcific discitis in an adult patient with intravertebral migration and spontaneous remission. *Skeletal Radiol.* **42**, 1161–1164. (doi:10.1007/s00256-013-1602-y)
16. Rodacki MA, Castro CE, Castro DS. 2005 Diffuse vertebral body edema due to calcified intraspongious disk herniation. *Neuroradiol. J.* **47**, 316–321. (doi:10.1007/s00234-004-1262-7)
17. Jin C, Frayssinet P, Pelker R, Cwirka D, Hu B, Vignery A, Eisenbarth SC, Flavell RA. 2011 NLRP3 inflammasome plays a critical role in the pathogenesis of hydroxyapatite-associated arthropathy. *Proc Natl Acad Sci USA* **108**, 14 867–14 872. (doi:10.1073/pnas.1111101108)
18. Feinberg J, Boachie-Adjei O, Bullough PG, Boskey AL. 1990 The distribution of calcific deposits in intervertebral discs of the lumbosacral spine. *Clin. Orthop. Relat. Res.* **254**, 303–310. (doi:10.1097/00003086-199005000-00046)
19. Dieppe PA, Crocker P, Huskisson EC, Willoughby DA. 1976 Apatite deposition disease: a new arthropathy. *Lancet* **1**, 266–269. (doi:10.1016/S0140-6736(76)91400-8)

Downloaded from https://royalsocietypublishing.org/ on 24 June 2025

20. Melrose J, Burkhardt D, Taylor TKF, Dillon CT, Read R, Cake M, Little CB. 2009 Calcification in the ovine intervertebral disc: a model of hydroxyapatite deposition disease. *Eur. Spine J.* **18**, 479–489. (doi:10.1007/s00586-008-0871-y)
21. Henmi A, Okata H, Anada T, Yoshinari M, Mikami Y, Suzuki O, Sasano Y. 2016 Bone matrix calcification during embryonic and postembryonic rat calvarial development assessed by SEM–EDX spectroscopy, XRD, and FTIR spectroscopy. *J. Bone Miner. Metab.* **34**, 41–50. (doi:10.1007/s00774-014-0647-x)
22. Lotsari A, Rajasekharan AK, Halvarsson M, Andersson M. 2018 Transformation of amorphous calcium phosphate to bone-like apatite. *Nat. Commun.* **9**, 4170. (doi:10.1038/s41467-018-06570-x)
23. Mahamid J, Sharir A, Addadi L, Weiner S. 2008 Amorphous calcium phosphate is a major component of the forming fin bones of zebrafish: indications for an amorphous precursor phase. *Proc Natl Acad Sci USA* **105**, 12 748–12 753. (doi:10.1073/pnas.0803354105)
24. Nitiputri K, Ramasse QM, Autefage H, McGilvery CM, Boonrungsiman S, Evans ND, Stevens MM, Porter AE. 2016 Nanoanalytical electron microscopy reveals a sequential mineralization process involving carbonate-containing amorphous precursors. *ACS Nano* **10**, 6826–6835. (doi:10.1021/acsnano.6b02443)
25. Brisson BA, Moffatt SL, Swayne SL, Parent JM. 2004 Recurrence of thoracolumbar intervertebral disk extrusion in chondrodystrophic dogs after surgical decompression with or without prophylactic fenestration: 265 cases (1995-1999). *J. Am. Vet. Med. Assoc.* **224**, 1808–1814. (doi:10.2460/javma.2004.224.1808)
26. Freeman P, Jeffery ND. 2017 Re-opening the window on fenestration as a treatment for acute thoracolumbar intervertebral disc herniation in dogs. *J. Small Anim. Pract.* **58**, 199–204. (doi:10.1111/jsap.12653)
27. Irfan M, Suprajaa PS, Baraneedharan P, Reddy BM. 2020 A comparative study of nanohydroxyapetite obtained from natural shells and wet chemical process. *J. Mater. Sci. Surf. Eng.* **7**, 938–943.
28. Garskaite E, Gross KA, Yang SW, Yang TC, Yang JC, Kareiva A. 2014 Effect of processing conditions on the crystallinity and structure of carbonated calcium hydroxyapatite (CHAp). *CrystEngComm.* **16**, 3950–3959. (doi:10.1039/c4ce00119b)
29. Koutsopoulos S. 2002 Synthesis and characterization of hydroxyapatite crystals: a review study on the analytical methods. *J. Biomed. Mater. Res* **62**, 600–612. (doi:10.1002/jbm.10280)
30. Mecozzi M, Sturchio E. 2017 Computer assisted examination of infrared and near infrared spectra to assess structural and molecular changes in biological samples exposed to pollutants: a case of study. *J. Imaging* **3**, 11. (doi:10.3390/jimaging3010011)
31. Ji Y, Yang X, Ji Z, Zhu L, Ma N, Chen D, Jia X, Tang J, Cao Y. 2020 DFT-calculated IR spectrum amide I, II, and III band contributions of N-methylacetamide fine components. *ACS Omega* **5**, 8572–8578. (doi:10.1021/acsomega.9b04421)
32. Schädle T, Pejcic B, Mizaikoff B. 2016 Monitoring dissolved carbon dioxide and methane in brine environments at high pressure using IR-ATR spectroscopy. *Anal. Methods* **8**, 756–762. (doi:10.1039/C5AY02744F)
33. Mehrotra R. 2000 Infrared spectroscopy, gas chromatography/Infrared in food analysis. In *Encyclopedia of analytical chemistry* (ed. RA Meyers), pp. 1–8. New York, NY: John Wiley & Sons.
34. Mansur HS, Sadahira CM, Souza AN, Mansur AA. 2008 FTIR spectroscopy characterization of poly (vinyl alcohol) hydrogel with different hydrolysis degree and chemically crosslinked with glutaraldehyde. *Mater. Sci. Eng. C* **28**, 539–548. (doi:10.1016/j.msec.2007.10.088)
35. Gadaleta SJ, Paschalis EP, Betts F, Mendelsohn R, Boskey AL. 1996 Fourier transform infrared spectroscopy of the solution-mediated conversion of amorphous calcium phosphate to hydroxyapatite: new correlations between X-ray diffraction and infrared data. *Calcif. Tissue Int.* **58**, 9–16. (doi:10.1007/BF02509540)
36. Eisa M, Al Dabbas M, Abdulla F. 2015 Quantitative identification of phosphate using X-ray diffraction and Fourier transform infrared (FTIR) spectroscopy. *Int. J. Curr. Microbiol. Appl. Sci.* **4**, 270–283.
37. Hellenbrandt M. 2004 The inorganic crystal structure database (ICSD) present and future. *Crystallogr. Rev.* **10**, 17–22. (doi:10.1080/08893110410001664882)
38. Sudarsanan K, Young RA. 1969 Significant precision in crystal structural details: holly springs hydroxyapatite. *Acta Cryst.* **25**, 1534–1543. (doi:10.1107/S0567740869004298)

39. Piazza RD, Pelizaro TA, Rodriguez-Chanfrau JE, La Serna AA, Veranes-Pantoja Y, Guastaldi AC. 2020 Calcium phosphates nanoparticles: the effect of freeze-drying on particle size reduction. *Mater. Chem. Phys.* **239**, 122004. (doi:10.1016/j.matchemphys.2019.122004)
40. Kourkoumelis N, Tzaphlidou M. 2010 Spectroscopic assessment of normal cortical bone: differences in relation to bone site and sex. *Sci. World J.* **10**, 402–412. (doi:10.1100/tsw.2010.43)
41. Ratner BD, Hoffman AS, Schoen FJ, Lemons JE. 2004 *Biomaterials science: an introduction to materials in medicine*, 2nd ed. Amsterdam, The Netherlands: Elsevier Academic Press Amsterdam.
42. Rey C, Shimizu M, Collins B, Glimcher MJ. 1991 Resolution-enhanced Fourier transform infrared spectroscopy study of the environment of phosphate ion in the early deposits of a solid phase of calcium phosphate in bone and enamel and their evolution with age: 2. Investigations in the nu3PO4 domain. *Calcif. Tissue Int.* **49**, 383–388. (doi:10.1007/BF02555847)
43. Londoño-Restrepo SM, Jeronimo-Cruz R, Millán-Malo BM, Rivera-Muñoz EM, Rodriguez-García ME. 2019 Effect of the nano crystal size on the X-ray diffraction patterns of biogenic hydroxyapatite from human, bovine, and porcine bones. *Sci. Rep.* **9**, 5915. (doi:10.1038/s41598-019-42269-9)
44. Yenen TB *et al.* 2025 Mineral phase changes during intervertebral disc degeneration. Figshare. (doi:10.6084/m9.figshare.c.7765060)

Downloaded from https://royalsocietypublishing.org/ on 24 June 2025